EFFECT OF HONEYCOMB STRUCTURE LAYOUT ON HEAT TRANSFER PERFORMANCE OF A HIGH-TEMPERATURE WIND TUNNEL STORAGE HEATER

Bao YANG[1], Hui YANG[1], Chen ZHANG[2]*, Weijie LIU[3] and Jiaxin YUAN[1]

[1] College of Air Transportation, Shanghai University of Engineering Science, Shanghai

[2] School of Aeronautics and Astronautics, Shanghai Jiao Tong University, Shanghai

[3] Institute of High-Speed, China Aerodynamics Research and Development Center, Mianyang

* Corresponding author. E-mail: piressjtu@sjtu.edu.cn

To meet the demand for stable high-temperature air sources in hypersonic ground testing, this study employs three-dimensional unsteady conjugate heat transfer simulations to investigate the thermo-fluid performance of honeycomb regenerators with different pore densities under constant porosity and pitch-to-diameter ratio constraints. The results show that the high-density configuration exhibits the best thermal output and sustained heat-supply capability. At the end of 120 s of discharge, its outlet temperature is 74 K higher than that of the low-density configuration, while its outlet-temperature drop over 60-120 s is reduced by 39%. At 120 s, its solid-temperature non-uniformity decreases from 18% in the upstream section to 1.7% in the downstream section. Under high-flow conditions, the high-density configuration also shows lower sensitivity to flow-rate disturbances and achieves a 13% improvement in energy extraction efficiency. However, this thermal advantage is accompanied by a greater flow penalty, with an average resistance coefficient 2 times that of the low-density configuration.

Keywords*: Regenerative heater, Honeycomb layout, heat transfer performance, Numerical simulation*

1. Introduction

Regenerative heaters are critical for ground testing of hypersonic vehicles and scramjets, providing stable high-enthalpy airflow for flight simulations [1]. As shown in Fig. 1, the heater comprises a shell, insulation layers, a regenerator core, and heating units, with dual-end inlets/outlets enabling fluid circulation during charging/discharging phases. High-purity test gas is essential, requiring minimal contamination to avoid data deviations. Unlike combustion or arc heaters that introduce H_2O, CO_2, and NOx, regenerative heaters deliver clean high-temperature gas [2]. Honeycomb storage units, offering excellent thermal performance, are widely used in high-temperature wind tunnels. Since internal channel configuration directly dictates heat transfer efficiency and flow resistance, its optimization has become a research focus.

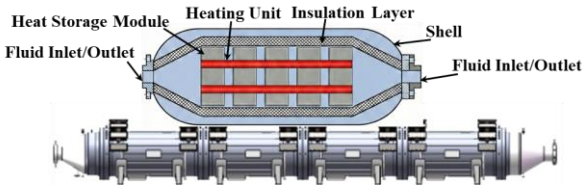

Figure 1. Schematic structure of the heater assembly

Previous studies have confirmed geometric modification as an effective means to enhance convective heat transfer. Dimpled structures disturb the boundary layer and improve local thermal performance [3], with compound arrangements further demonstrating the sensitivity of heat transfer to geometric configuration [4]. Ball turbulators strengthen fluid mixing [5], while twisted tapes [6] and corrugated tubes [7] serve as effective continuous inserts for thermal enhancement. Multi-parameter optimization studies have shown that geometric design can further improve overall thermo-hydraulic performance [8]. More recently, vortex-inducing microstructures and rib-type structures have been found to significantly enhance local heat transfer by generating secondary flow and disrupting the thermal boundary layer [9]—rectangular vortex generators induce multi-longitudinal swirls [10], and rib-type microstructures intensify near-wall transport [11]. These studies clearly demonstrate the importance of geometry in controlling thermo-fluid performance. However, most of these strategies were developed for single tubes or simple channels and are difficult to manufacture inside dense ceramic honeycomb regenerators. Therefore, optimizing the macroscopic honeycomb layout is more practical than introducing complex internal turbulators for the present application.

Although evaluating macroscopic thermal performance is critical, current regenerator analyses still heavily rely on simplified models. Classical 1D methods neglect radial gradients [12], and micro-scale analyses often isolate adiabatic single channels [13]. However, these simplifications fail to capture severe cross-sectional flow maldistributions [14]. As demonstrated by Choi et al. [15] and Carbonare et al. [16], neglecting 3D transient effects causes prediction errors exceeding 20%, artificially overestimating heat recovery performance while dangerously underestimating thermal decay risks. Accordingly, a full-scale 3D unsteady analysis is indispensable for accurately resolving the thermo-fluid degradation in practical regenerative heaters.

Consequently, existing research lacks full-scale 3D characterizations of honeycomb regenerators under realistic boundaries, leaving the nonlinear impacts of macroscopic layouts on thermo-fluid degradation unclear. To address this, the present study develops a full-scale 3D unsteady conjugate heat transfer (CHT) model for a high-temperature wind-tunnel regenerative heater. By evaluating varying hole densities at a constant porosity, this study elucidates how cross-sectional configurations govern internal flow uniformity, outlet temperature stability, and effective operating duration. Ultimately, these findings provide theoretical guidance for optimizing large-scale regenerators in engineering practice.

2. Physical model and thermal physical properties

2.1. Physical model

As shown in Fig. 2, a physical model was established based on a prototype regenerative heater for a hypersonic wind tunnel. To investigate the effect of honeycomb layout on thermo-fluid performance, three array configurations with different hole number densities were considered: Case 1 (N = 10, d = 25 mm), Case 2 (N = 19, d = 18.15 mm), and Case 3 (N = 37, d = 13 mm). For consistency, the cross-sectional porosity (ε = 30%) and pitch-to-diameter ratio (s/d = 1.52) were kept constant.

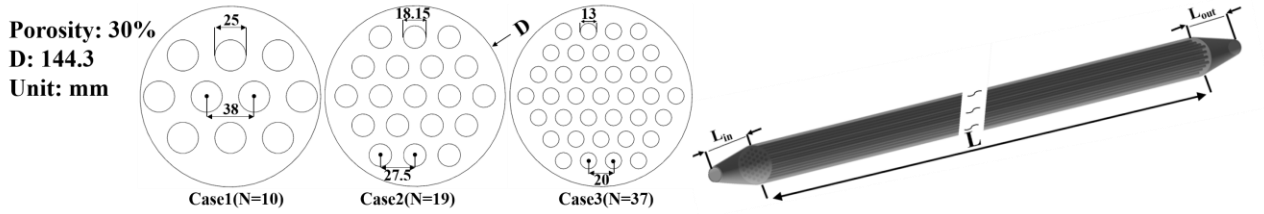

Figure 2. Schematic of the full-scale 3D geometric model and cross-sectional honeycomb layouts

The 3D model comprises a core regenerator 20 m in length and 144.3 mm in diameter, encased within a 3 mm thick solid shell. To replicate realistic flow conditions, upstream and downstream settling chambers (200 mm long, 55 mm inlet/outlet diameter) were incorporated at both ends. Furthermore, inlet boundary conditions were equivalently scaled based on the flow-area ratio to ensure the internal mass flow rate matches the operational parameters of the prototype.

2.2. Thermophysical properties and operating conditions

The regenerator matrix is made of S30408 stainless steel. Under the 950 K preheating condition, temperature-dependent thermophysical properties are critical to the unsteady heat storage and release process. In this paper, the specific heat capacity and thermal conductivity are defined as:

$$C_{\mathrm{p}} = 0.1553T + 448.53 \tag{1}$$

$$\lambda = 0.014T + 10.878 \tag{2}$$

Here, C_{p} is the specific heat capacity [J kg^{-1}K^{-1}], λ is the thermal conductivity [W m^{-1}K^{-1}], and T is the temperature [K]. Throughout the following text, the subscripts f and s, when used, denote the fluid and solid, respectively.

Because the temperature dependence of density is negligible, the material density is taken as a constant 7582 kg/m³. Numerical simulations are performed using the geometric models described above. Following the prototype rated condition, the operating pressure is set to 6 MPa, with an inlet air temperature of 273.15 K and an initial preheating temperature of 950 K. Using the nominal mass flow rate of 609 kg/s as the baseline, two additional cases at ±20% (487 and 731 kg/s) are considered.

3. Numerical modeling and solution strategy

3.1. Governing equations

To capture the 3D unsteady thermo-fluid coupling within the heater, the high-temperature, high-pressure working fluid is modeled as an ideal gas. Neglecting gravity and radiation, the governing conservation equations for the fluid and solid domains are given by [17]:

$$\rho_{\mathrm{f}} C_{\mathrm{p,f}} \frac{\partial T_{\mathrm{f}}}{\partial t} + \rho_{\mathrm{f}} C_{\mathrm{p,f}} (\vec{u} \cdot \nabla) T_{\mathrm{f}} = \nabla \cdot (\lambda_{\mathrm{f}} \nabla T_{\mathrm{f}}) \tag{3}$$

$$\frac{\partial (\rho_{\mathrm{s}} C_{\mathrm{p,s}} T_{\mathrm{s}})}{\partial t} = \nabla \cdot (\lambda_{\mathrm{s}} \nabla T_{\mathrm{s}}) \tag{4}$$

$$\frac{\partial \rho_{\mathrm{f}}}{\partial t} + \nabla \cdot (\rho_{\mathrm{f}} \vec{u}) = 0 \tag{5}$$

$$\rho_{\mathrm{f}} \frac{\partial \vec{u}}{\partial t} + \rho_{\mathrm{f}} (\vec{u} \cdot \nabla) \vec{u} = -\nabla p + \nabla \cdot \left[\mu_{\mathrm{f}} \left(\nabla \vec{u} + (\nabla \vec{u})^{\mathrm{T}} - \frac{2}{3} (\nabla \cdot \vec{u}) \mathbf{I} \right) \right] \tag{6}$$

where ρ is the density [kg m^{-3}], $\vec{u}$ is the fluid velocity vector, p is the pressure [Pa], μ is the dynamic viscosity, and $\mathbf{I}$ is the identity tensor.

3.2. Boundary conditions, mesh generation and numerical methods

As shown in Fig. 3, the computational domain was discretized using a multi-block structured hexahedral mesh and includes both fluid and solid regions. An O-grid topology was adopted in each cross-section to fit the circular honeycomb channels and improve mesh quality. Local refinement was applied near the fluid-solid interface and the wall region to resolve the steep velocity and temperature gradients. The boundary conditions consist of a mass-flow inlet and a pressure outlet. Conjugate heat transfer was achieved by treating the fluid-solid interface as a coupled wall, while natural convection at the outer wall was modeled using the Churchill-Chu correlation with a heat transfer coefficient of 8 W/(m²·K).

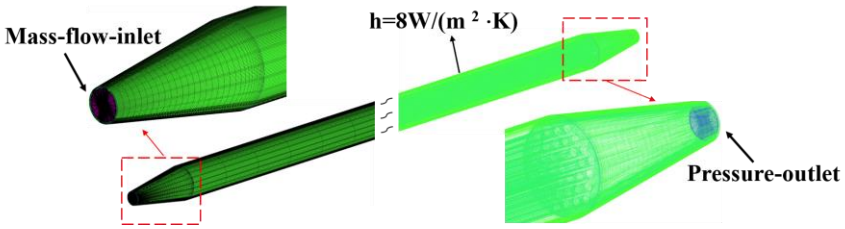

Figure 3. Computational mesh and boundary conditions

The governing equations were discretized and solved using the finite volume method (FVM), with an implicit pressure-based solver employed for the flow field. Second-order upwind schemes were used for the momentum, energy, and turbulence equations to improve numerical accuracy. The convergence criteria were set to 1E-6 for the energy residual and 1E-4 for the residuals of the continuity, momentum, and other governing equations. In addition, the inlet and outlet mass flow rates were monitored throughout the calculation to ensure strict satisfaction of mass conservation at convergence.

3.3. Grid independence and validation

A grid independence study was performed using the convective heat transfer coefficient (HTC) and pressure drop as monitoring indicators. Taking the Case 3 configuration, which has the most complex geometry, as the benchmark, five sets of structured grids with sizes of 1.68 million – 6.20 million cells were created. As shown in Fig. 4, the monitoring indicators stabilize asymptotically with increasing grid number. When the grid size reaches 5.0 million cells, further refinement has negligible impact on the results, confirming grid independence. To balance computational resources and accuracy, a grid strategy of 5.0 million cells was adopted for all subsequent simulations. The remaining configurations followed the same grid generation criteria to ensure consistency.

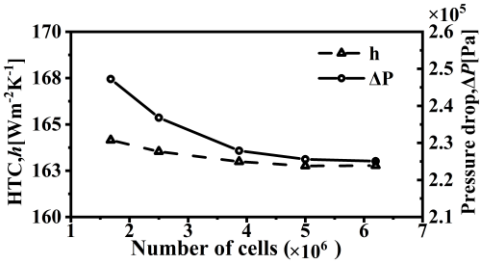

Figure 4. Grid independence validation results

To validate the numerical method, the simulation setup was established according to the parameters reported in Reference [18]. The purpose of this validation case was to assess the capability of the present numerical method to reproduce the transient thermal evolution inside the regenerator passage during the heating process. The computational domain was simplified to a channel model with

a length of 5.5 m and a diameter of 8 mm. The regenerator material was modeled as alumina with temperature-dependent properties. The initial temperature was set to 300 K, the inlet air temperature to 600 K, and the inlet mass flow rate to 2 kg/s.

As shown in Fig. 5, the simulated axial temperature distributions agree well with the experimental data, accurately capturing the transient thermal evolution at 1 h, 3 h, and 5 h. At the late heating stage (5 h), a slight underprediction appears in the inlet region (z < 1 m). This deviation is primarily attributed to the simplification of alumina thermal properties as first-order linear functions, the idealized boundary conditions compared to the complex experimental environment, and potential uncertainties in the precise spatial positioning of measurement sensors. Nevertheless, the maximum relative deviation remains below 5%, confirming the accuracy and reliability of the numerical method adopted in this study.

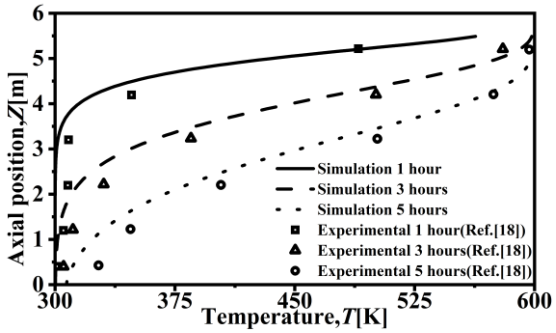

Figure 5. Comparison of experimental and numerical results for the axial temperature distribution of the regenerator at different heating times

3.4. Evaluation indices for heat transfer and hydraulic resistance performance

Inspired by the thermodynamic treatment in Ref. [19], the energy extraction efficiency (η) is defined as the ratio of the cumulative heat absorbed by the fluid during the operating time (t_{op}) to the maximum theoretical sensible heat available in the solid matrix:

$$\eta = \frac{E_{\text{extracted}}}{E_{\text{stored}}} = \frac{\int_0^{t_{op}} \dot{m}[h_f(\bar{T}_{out}(t)) - h_f(T_{in})]\mathrm{d}t}{M_s[h_s(T_{ini}) - h_s(T_{in})]} \tag{7}$$

where $\dot{m}$ is the fluid mass flow rate [kg s^{-1}], Ms is the total mass of the solid matrix [kg]. $\bar{T}_{out}(t)$ is the area-weighted average temperature at the outlet section, T_{ini} is the initial temperature of the solid matrix, T_{in} is the inlet temperature of the airflow, and t_{op} is the operating time[s]. The specific enthalpy $h(T)$ is calculated by integrating the temperature-dependent specific heat capacity $C_p(T)$:

$$h(T) = \int_{T_{in}}^{T} C_p(T)\mathrm{d}T \tag{8}$$

For the discrete data, $E_{\text{extracted}}$ is calculated using the trapezoidal rule [20], with Δt = 1 s.

$$E_{\text{extracted}} \approx \sum_{i=1}^{N_t-1} \dot{m}\frac{\Delta h(t_i) + \Delta h(t_{i+1})}{2}\Delta t \tag{9}$$

where $\Delta h(ti)$ represents the enthalpy difference relative to the inlet temperature at time t_i. N_t is the number of time steps.

The flow resistance performance is evaluated using the time averaged pressure drop over the operating period.

The cross-sectional temperature non-uniformity coefficient is introduced following Ref. [21]:

$$\mathrm{RSD}_T = \left[\sum_{i=1}^{n} A_i(T_i - \bar{T})^2 / \sum_{i=1}^{n} A_i\right]^{1/2} / \bar{T} \tag{10}$$

where A_i is the area of the i-th surface element, T_i is its temperature, $\bar{T}$ is the area-weighted mean cross-sectional temperature, and n is the total number of discrete surface elements.

Condensation occurs within the nozzle when stagnation temperature falls below the critical value, degrading flow quality. Based on Eq. (11), the minimum total temperature required to prevent flow condensation can be calculated for various Mach numbers at a given total pressure[22].

$$\lg p_0 - \gamma \lg\left(1+\frac{\gamma-1}{2}M^2\right)/(\gamma-1) = B - A\left(1+\frac{\gamma-1}{2}M^2\right)/T_0 \tag{11}$$

where p_0 is the total pressure, T_0 is the total temperature, M is the Mach number, A = 336.34 K, and B = 9.32. γ is the specific heat ratio of the gas.

4. Results and analysis

4.1. Impact of different honeycomb layouts on heat transfer and flow resistance performance

Figure 6 compares the transient outlet temperature of the three configurations during a 120 s discharge at 3.08 kg/s. All cases show a nonlinear decay as the stored heat in the matrix is depleted. In the initial stage (t < 20 s), the curves are close because the outlet response is mainly controlled by the release of the initially stored heat. As the discharge proceeds, the difference becomes more evident. A higher hole count increases the gas-solid contact perimeter and reduces the heat conduction distance inside the matrix. Therefore, after the near-wall heat is consumed, thermal energy stored in the interior can be transferred to the wall region more continuously. This slows the wall temperature drop and helps sustain heat transfer to the flow. As a result, the high-hole-count configuration maintains a higher outlet temperature and a lower decay rate. At t = 120 s, Case 3 reaches 887 K, while Case 1 drops to 813 K. From 60 to 120 s, the temperature drop is 82 K for Case 1 but only 50 K for Case 3. This indicates that increasing the hole count improves not only the heat-release level, but also the continuity of heat supply during discharge, thereby enhancing output stability.

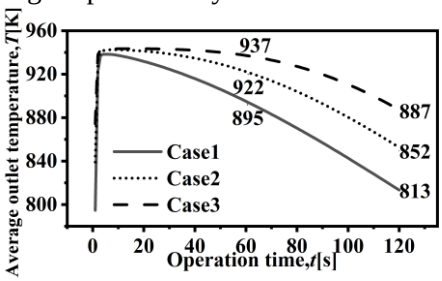

Figure 6. Temporal evolution of the average outlet temperature for cases at 3.08 kg/s

To identify the physical origin of the outlet-temperature difference, Fig. 7 presents cross-sectional temperature contours at t = 60 s and 120 s for Z/L = 0.1, 0.5, and 0.9, covering the upstream, middle, and downstream regions during intermediate and late discharge. The downstream region corresponds to the outlet temperature, which is the main engineering concern, while the upstream and middle regions are used to evaluate the axial development of heating performance.This reveals how sectional heating evolves in time and space. In Case 1, a clear cold-core/hot-rim pattern appears near the inlet, indicating heating is concentrated near the wall while the core remains underheated. This arises from coupled flow penetration and solid heat replenishment: the core fluid has shorter thermal interaction time due to more direct passage through the center, while the coarse structure lengthens the solid conduction path, limiting heat replenishment after near-surface heat is consumed. Thus, the wall remains the main heat-release zone. Downstream, this radial non-uniformity weakens as heat transfers from the hot rim toward the

core. In contrast, Case 3 exhibits stronger downstream heating, suggesting that increasing hole count improves the continuity of heat supply from the solid matrix. This trend is also consistent with the degree of air heating: at 60 s, ΔT increases from 608 K in Case 1 to 635 K in Case 2 and 652 K in Case 3. at 120 s, the values are 534, 574, and 610 K, respectively. These results indicate that a higher hole count delays local thermal depletion and sustains stronger heat release during discharge.

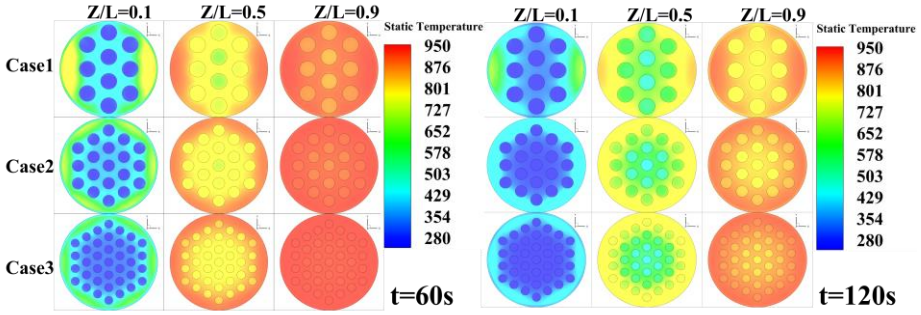

Figure 7. Spatiotemporal static temperature contours for cases

The solid-temperature non-uniformity is quantified by the RSD_T, and the results at different axial positions and discharge times are listed in Table 1. At both 60 s and 120 s, the non-uniformity is highest in the upstream section and lowest in the downstream section, indicating that the solid-temperature field becomes more uniform along the flow direction. For example, at 60 s, the RSD_T at the upstream position (Z/L = 0.1) ranges from 20% to 26%, whereas it decreases to only 0.15%–0.9% at the downstream position (Z/L = 0.9). At 120 s, the corresponding ranges are 18%–27% upstream and 1.7%–2.7% downstream. Meanwhile, the trends in the upstream and middle sections are not monotonic, whereas the high-density configuration consistently shows the lowest non-uniformity in the downstream section, with the RSD_T being only 0.15% at 60 s and 1.7% at 120 s. This behavior is governed by gas-solid heat transfer and internal solid conduction during flow development. Heat release is stronger in the upstream region, so the cross-sectional temperature gradient is more pronounced. As the flow develops downstream, the gas-solid temperature difference decreases, weakening the local heat-release driving force. Meanwhile, internal solid conduction transfers heat from high-temperature regions to low-temperature regions, reducing the cross-sectional temperature difference and promoting temperature uniformity. As a result, the high-density configuration, with its shorter conduction path and more distributed heat-release interfaces, alleviates local thermal depletion in the terminal region and maintains a more uniform solid-temperature field, leading to a slower decay of outlet temperature.

Table 1. Solid-temperature non-uniformity at different axial positions and times

Time	Axial position	Case1	Case2	Case3
t = 60s	Z/L=0.1	20%	23%	26%
	Z/L=0.5	5%	4.8%	4.3%
	Z/L=0.9	0.9%	0.45%	0.15%
t = 120s	Z/L=0.1	27%	20%	18%
	Z/L=0.5	10%	10.7%	12.3%
	Z/L=0.9	2.7%	2.4%	1.7%

In this section, the pressure drop is normalized by the instantaneous inlet dynamic pressure to obtain the resistance coefficient. Fig. 8 shows that the resistance coefficient increases with hole count

and decreases gradually during discharge. This indicates that, under the same flow reference, the high-density configuration imposes a stronger flow resistance. The reason is that, at the same porosity, increasing the hole count refines the passage structure and increases the wetted perimeter and gas-solid contact area, thereby strengthening wall-friction loss. Meanwhile, the gradual decrease in resistance coefficient reflects the continuous weakening of flow resistance during discharge. At the initial stage, the gas temperature is high, resulting in a larger dynamic viscosity and stronger viscous resistance. At the same time, the low gas density at high temperature requires a higher flow velocity to maintain the same mass flow rate, making inertial loss more pronounced. As discharge proceeds, the gas temperature decreases, so the viscosity drops, the density recovers, and the flow velocity is reduced. Consequently, both viscous and inertial losses weaken, leading to a gradual decline in the resistance coefficient.

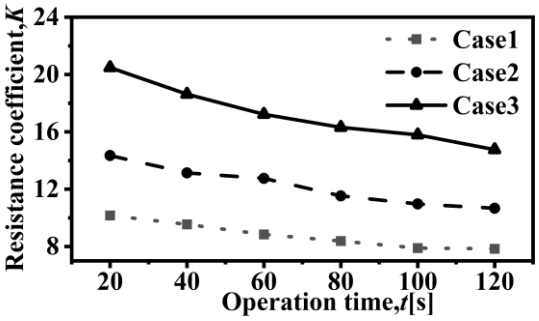

Figure 8. Temporal evolution of the average resistance coefficient for cases

4.2. Impact of mass flow rate on flow resistance and heat transfer performance

Figure 9 compares transient outlet temperature responses of three configurations under varying inlet mass flow rates. In all cases, higher flow rates accelerate outlet temperature decay, indicating weakened temperature maintenance during discharge. This trend arises from a dynamic imbalance: while increased velocity enhances gas-solid convection, it also raises the gas heat-capacity rate, distributing finite bed heat over more fluid and reducing per-unit temperature rise. Simultaneously, shorter residence time limits full heat absorption before discharge. Thus, despite convection enhancement, outlet temperature declines faster when internal conduction and heat release cannot sustain the near-outlet high-temperature zone, allowing the thermal front to advance more rapidly.

Distinct early-stage behaviors emerge across cases. In Case 1, temperature curves diverge immediately after discharge starts, with higher flow rates causing steeper drops—revealing high sensitivity to flow perturbations and weak heat delivery from storage to outlet. Case 3, however, exhibits pronounced flow-rate independence initially (t < 20 s): curves under different flows nearly overlap, maintaining a stable high-temperature plateau. This suggests its pore structure enables uniform early heat release, buffering against flow disturbances and delaying temperature decay. Overall, Case 3 demonstrates superior thermal buffering and high-temperature retention during the initial transient.

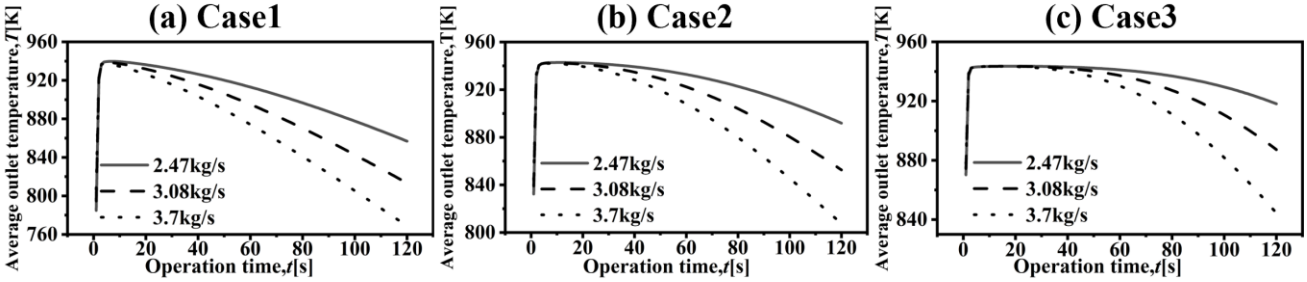

Figure 9. Temporal evolution of outlet gas temperature under varying $\dot{m}$ for cases

To clarify the heat-transfer mechanisms behind the outlet-temperature response, Fig. 10 shows the internal temperature distributions of Case 1 and Case 3 at t=20 s under different mass flow rates, with a selected section illustrating the axial temperature evolution in the regenerator.

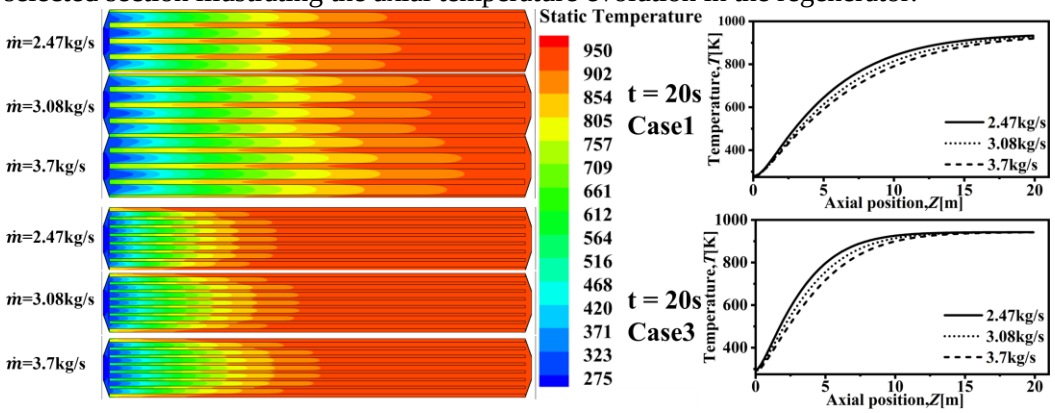

Figure 10. Internal temperature distributions of Cases 1 and 3 at t = 20 s under different inlet flow rates: (left) longitudinal contours, (right) axial temperature profiles along the centerline.

For Case 1, the longitudinal temperature contours show that the thermal front penetrates further downstream as the mass flow rate increases. Consistently, the axial temperature profiles indicate lower downstream fluid temperatures, with the three curves remaining clearly separated near the outlet. This suggests that, in Case 1, the gas heating process is still incomplete within the finite channel length, making the outlet temperature highly sensitive to flow rate. The main reason is that its smaller specific surface area limits gas-solid heat transfer. At higher flow rates, although convection is enhanced, the gas heat-capacity flow rate increases and the residence time decreases, so the gas still cannot approach thermal equilibrium with the solid matrix before leaving the channel. As a result, the thermal front is stretched and shifts further toward the outlet.

For Case 3, the thermal front shifts downstream with increasing flow rate, but the axial temperature profiles show distinct behavior. Although the curves separate in the upstream region, they nearly collapse at the downstream end (Z>15 m) and remain close to the maximum temperature. This indicates that most gas heating is completed in the upstream-to-midstream region, where the gas has approached thermal equilibrium with the matrix, leaving little room for further temperature rise. This behavior arises from the larger specific surface area of Case 3, which strengthens gas-solid heat transfer in the inlet region and allows the gas to absorb heat rapidly over a short distance. At lower flow rates, this equilibrium position is reached earlier. At higher flow rates, it is delayed, but the downstream plateau is preserved. Therefore, the outlet temperature is less sensitive to flow-rate changes.

A comparison shows that, under the same high-flow condition, the thermal front in Case 1 extends to about three-quarters of the channel length and approaches the outlet, whereas in Case 3 it remains mainly confined to roughly the upstream half. This indicates that the high-surface-area structure strengthens upstream heat transfer and shortens the axial distance required for the main temperature rise, suppressing thermal-front migration toward the outlet and improving outlet-temperature stability.

Figure 11 shows the variations of energy extraction efficiency and cycle-averaged resistance coefficient with mass flow rate. As the mass flow rate increases, the energy extraction efficiency rises for all three configurations. Although a higher flow velocity shortens the residence time and reduces the temperature rise of the fluid per unit mass, the increase in mass flow rate is more dominant. As a result, the total heat extracted per unit time still increases, leading to a higher overall energy extraction efficiency. By contrast, the cycle-averaged resistance coefficient decreases with increasing mass flow

rate, while the difference among configurations remains clear, with Case 3 showing the highest averaged resistance coefficient over the entire flow-rate range. This is because its structure is the most compact, with a larger specific surface area and smaller pore passages, causing more frequent contraction, expansion, and flow redistribution within the pore network. These features intensify local flow separation and form drag, thereby maintaining a higher overall flow resistance.

A cross-case comparison reveals a clear trade-off between thermal gain and flow penalty. At 3.7 kg/s, Case 3 improves energy extraction efficiency by 3.49 percentage points over Case 1, but its averaged resistance coefficient is twice that of Case 1, indicating a significantly higher pumping-power requirement. Thus, microstructural enhancement improves heat transfer at the cost of higher flow resistance, so practical design must balance thermal performance against operating cost. For wind-tunnel heater design, the high-density configuration is preferable when thermal stability and sustained high-temperature output are prioritized; the low-density configuration suits lower pressure drop and pumping-power demand, while the intermediate configuration offers a compromise.

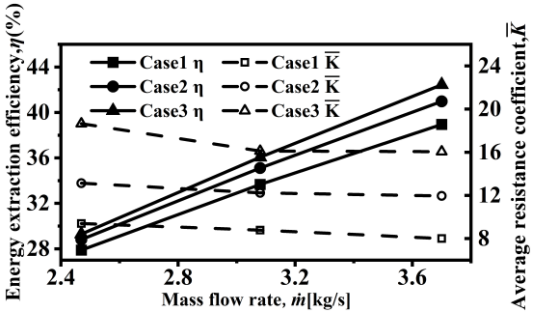

Figure 11. Energy extraction efficiency and average resistance coefficient versus ṁ for cases

4.3. Assessment of operational stability: evolution patterns of effective operating time

The effective operating time, t_{eff}, is defined as the duration for which the outlet temperature remains above a prescribed threshold. To meet the wind-tunnel demand for a stable heat source, heating performance in this section is evaluated using t_{eff} as the primary metric. For the Mach 9, 6 MPa condition, the heater-outlet temperature threshold was obtained by substituting the required freestream parameters into Eq. (11), converting the wind-tunnel test requirement into the minimum outlet-temperature requirement of the heater. The resulting threshold is approximately 842 K, below which the test requirement would be difficult to satisfy. Quantitatively, t_{eff} decreases with increasing mass flow rate for all configurations, but their resistance differs markedly. Case 3 maintains the outlet temperature above the threshold across the flow-rate range, achieving full-cycle compliance. By contrast, t_{eff} for Case 1 drops to 99 s and 78 s at medium and high flow rates, while Case 2 shortens to 101 s at high flow.

This occurs because increasing flow rate intensifies instantaneous energy extraction from the matrix, placing stringent demands on heat transfer. With smaller specific surface areas, Cases 1 and 2 cannot supply heat fast enough to match the elevated demand, causing premature temperature drop. In comparison, the large specific surface area of Case 3 enables efficient solid–fluid energy compensation even under intense extraction, thereby improving thermal stability during high-load operation.

5. Conclusions

This study developed a three-dimensional transient numerical model to investigate the thermo-fluid performance of honeycomb regenerators with different pore densities in a hypersonic wind tunnel heater. The outlet-temperature response, cross-sectional temperature distribution, internal temperature

evolution, energy extraction efficiency, and flow-resistance characteristics under different mass flow rates were systematically analyzed. The main conclusions are as follows:

(1) The high-density configuration exhibits higher thermal output and stronger sustained heat-supply capability. Under the same operating conditions, the final outlet temperature of Case 3 is 9.1% higher than that of Case 1, while the outlet-temperature drop during 60–120 s is reduced by about 39%. Meanwhile, the solid-temperature distribution in the downstream region is more uniform, indicating that the high-density configuration helps delay local thermal depletion and improve output stability.

(2) Increasing the mass flow rate accelerates the outlet-temperature decay of all configurations, whereas the high-density configuration is less sensitive to flow-rate disturbances. Under high-flow conditions, the energy extraction efficiency of Case 3 is about 13% higher than that of Case 1, and its outlet temperature remains more stable during the initial stage, indicating a stronger thermal buffering capability. Thus, the high-density design is preferable under variable-flow conditions.

(3) While the high-density configuration improves thermal performance, it also significantly increases flow resistance. Although Case 3 exhibits the best thermal performance over the entire flow-rate range, its average resistance coefficient is 2 times that of Case 1. Therefore, in practical design, a balance should be considered between heat-supply capability and resistance loss.

The conclusions were obtained under fixed porosity and pitch-to-diameter ratio for similar honeycomb arrays. Thus, caution is needed when extending them to other regenerator structures with significantly different geometries. Moreover, this study is mainly based on numerical simulations and does not account for radiation or material heterogeneity. Future work should incorporate experimental validation and extend the analysis to comprehensive optimization under a wider range of geometric parameters and practical operating conditions.

References

[1] Babu, S. N., et al., Selection of High Temperature Heat Storage Materials for Cored Brick Heaters of Hypersonic Wind Tunnel and Scramjet Facilities, *Materials Today: Proceedings*, 5 (2018), 2, pp. 7924-7929. DOI No. 10.1016/j.matpr.2017.11.474.

[2] Luo, F.-T., et al., Investigation of Cored Bricks Matrix Preliminary Design and Thermal Analysis for High Temperature Wind Tunnel Storage Heater, *Journal of Experiments in Fluid Mechanics*, 27 (2013), pp. 38-45.

[3] Al-Obaidi, A. R., Alhamid, J., Influence of Different Geometrical Dimple Configurations on Flow Behaviour and Thermal Performance within a 3D Circular Pipe, *Journal of Thermal Engineering*, 10 (2021), 1, pp. 175-187.

[4] Alhamid, J., et al., A Numerical Study to Investigate the Effect of Turbulators on Thermal Flow and Heat Performance of a 3D Pipe, *Heat Transfer*, 51 (2022), 3, pp. 2458-2475. DOI No. 10.1002/HTJ.22407.

[5] Al-Obaidi, A. R., et al., Flow Field Structure, Characteristics of Thermo-Hydraulic and Heat Transfer Performance Analysis in a Three Dimensions Circular Tube with Different Ball Turbulators Configurations, *Arabian Journal for Science and Engineering*, 46 (2021), 12, pp. 12253-12282. DOI No. 10.1007/S13369-021-05943-7.

[6] Al-Obaidi, A. R., Investigation of Thermal Flow Structure and Performance Heat Transfer in Three-Dimensional Circular Pipe Using Twisted Tape Based on Taguchi Method Analysis, *Heat Transfer*, 51 (2022), 2, pp. 1649-1667. DOI No. 10.1002/HTJ.22368.

[7] Al-Obaidi, A. R., Investigation Evaluation of Thermo-Hydraulic Flow and Heat Improvement in a 3D Circular Corrugated Pipe Based on Response Surface Method and Taguchi Analyses, *Heat and Mass Transfer*, 60 (2024), 4, pp. 573-597. DOI No. 10.1007/S00231-024-03456-1.
[8] Al-Obaidi, A. R., Thermal Flow and Heat Performance Analyses in Circular Pipe Using Different Twisted Tape Parameters Based on Design of Experiments, *Heat Transfer*, 51 (2022), 8, pp. 7202-7232. DOI No. 10.1002/HTJ.22641.
[9] Ikumapayi, O. M., et al., Optimizing Heat Transfer in Laminar Channel Flow Using Inclined Inverted L-Shaped Obstacles, *Thermal Science*, 29 (2025), 4 Part B, pp. 3219-3227. DOI No. 10.2298/TSCI2504219I.
[10] Zhu, S., et al., Investigations of Thermohydraulic Performance in Heat Exchanger Tube with Rectangular Vortex Generators, *Thermal Science*, 28 (2024), 4 Part A, pp. 2917-2928. DOI No. 10.2298/TSCI231127088Z.
[11] Wan, X., et al., Analysis of Heat Transfer Mechanisms in Microchannels with Different Vortex-Inducing Microstructures, *Thermal Science*, 00 (2025), pp. 121-121.
[12] Reznicek, E. P., et al., One-Dimensional, Transient Modeling of a Fixed-Bed Regenerator as a Replacement for Recuperators in Supercritical CO2 Power Cycles, *Energy Conversion and Management*, 218 (2020), 112921. DOI No. 10.1016/j.enconman.2020.112921.
[13] Liu, F., et al., Heat Transfer Characteristics in Regenerator Cell for Gaseous Organic Compound Treatment, *Journal of Mechanical Science and Technology*, 37 (2023), 2, pp. 1001-1010. DOI No. 10.1007/S12206-023-0139-9.
[14] Giuntini, L., et al., Coupled CFD and 1-D Dynamic Modeling for the Analysis of Industrial Regenerative Thermal Oxidizers, *Chemical Engineering and Processing: Process Intensification*, 157 (2020), 108117. DOI No. 10.1016/j.cep.2020.108117.
[15] Choi, Y., et al., How Can We Simulate the Bi-Directional Flow and Time-Variant Heat Exchange Ventilation System?, *Applied Thermal Engineering*, 181 (2020), 115948. DOI No. 10.1016/j.applthermaleng.2020.115948.
[16] Carbonare, N., et al., Simulation and Measurement of Energetic Performance in Decentralized Regenerative Ventilation Systems, *Energies*, 13 (2020), 22, 6010. DOI No. 10.3390/EN13226010.
[17] You, Y., et al., A Three-Dimensional Numerical Model of Unsteady Flow and Heat Transfer in Ceramic Honeycomb Regenerator, *Applied Thermal Engineering*, 108 (2016), pp. 1243-1250. DOI No. 10.1016/j.applthermaleng.2016.08.035.
[18] Besharati, M. T., et al., Design High Temperature Cored Brick Heater for Hypersonic Wind Tunnel, *Fluid Mechanics & Aerodynamics*, 9 (2020), 1, pp. 45-66.
[19] Liang, H., et al., Phase Change Material Thermal Energy Storage Design of Packed Bed Units, *Journal of Energy Storage*, 51 (2022), 104576.
[20] Sánchez-Orgaz, S., et al., A New Thermodynamic Model to Approximate Properties of Subcritical Liquids, *Entropy*, 25 (2023), 7, 1002. DOI No. 10.3390/E25071002.
[21] Wiberg, R., Lior, N., Heat Transfer from a Cylinder in Axial Turbulent Flows, *International Journal of Heat and Mass Transfer*, 48 (2005), 8, pp. 1505-1517. DOI No. 10.1016/j.ijheatmasstransfer.2004.10.015.
[22] Chen, J.-f., et al., Performance Parameter Computation of the Storage Heater in a General Hypersonic Wind Tunnel, *Journal of Experiments in Fluid Mechanics*, 26 (2012), 5, pp. 88-92.

RECEIVED DATE: 3.2.2026.
DATE OF CORRECTED PAPER: 27.2.2026
DATE OF ACCEPTED PAPER: 30.03.2026.